Journal of Materials Chemistry A

ROYAL SOCIETY OF CHEMISTRY

PAPER

Cite this: J. Mater. Chem. A, 2022, 10, 16620

Enhancement of the thermoelectric power factor in monolayer PbBiI: staggered exchange field effect

Le T. T. Phuong, [a] Tran C. Phong,[a] Bui D. Hoi *[a] and Mohsen Yarmohammadi [bc]

Received 19th April 2022
Accepted 11th July 2022

DOI: 10.1039/d2ta03132a

rsc.li/materials-a

The unique features of the monolayer PbBiI originate from the gapped and gapless states protected by the time-reversal symmetry. These states appear with the angular momenta $J = \{1/2, 3/2\}$. The engineering of thermoelectric performance in monolayer PbBiI is highly desirable due to the forbidden backscattering mechanism of electrons. Herein, a known physical staggered exchange field is implemented to calculate the Onsager transport coefficients within the Kubo–Greenwood framework. This, in turn, enhances the power factor (PF) through highly dispersive and degenerate energy bands resulting from the staggered exchange field. We report exceptional 133%, 53%, and 22% enhancements of PF at temperatures 480 K, 460 K, and 440 K, respectively, when we turn on the exchange field to act on $J = 3/2$, $J = 1/2$, and both Js. The predicted PFs propose a new research line to achieve the highest thermoelectric efficiency in low-dimensional materials.

1 Introduction

In conventional topological insulators, gapped and gapless states coexist,[1–4] which leads to unique conductive features.[5] In these systems, owing to the strong spin–orbit coupling (SOC), time-reversal symmetry is responsible for protecting gapless states.[6–8] Quantum spin Hall insulators (QSHIs) are two-dimensional (2D) versions of topological insulators with inherent SOC and band inversion[1–4] except that the gapless edge states are fully spin-polarized. This feature introduces them as potential candidates for quantum computing and spintronic purposes.[9–11]

Global climate change because of the combustion of fossil fuels is a pressing issue nowadays. In this regard, researchers are trying to increase the energy efficiency of thermoelectric materials for the largest waste-heat into electric conversion[12,13] and the search for high-performance materials is a subject of interest. The performance of thermoelectric materials at a given temperature T is typically determined by a dimensionless figure of merit $\mathcal{Z}T = \mathcal{P}T/\kappa$, where $\mathcal{P}$ is the power factor (PF) and κ is the total thermal conductivity (electronic and phononic). To achieve a high $\mathcal{Z}T$, the PF (thermal conductivity) should be increased (decreased). There are various ways to tune $\mathcal{Z}T$. In the work by Ding *et al.*,[14] a strategy has been proposed to utilize the overlap of p_z orbitals to increase the thermoelectric efficiency of a layered polymeric carbon nitride, which is a great guidance to search for layered materials with high cross-plane thermoelectric performance. In another study by Mi *et al.*,[15] a low-dimensional electronic structure is employed in bulk phonon-glass crystals as an alternative way to increase the thermoelectric efficiency. On the other hand, the reduction of the anisotropic temperature-dependent thermal conductivity of poly(3,4-ethylenedioxythiophene) with different doping concentrations has been addressed by molecular dynamics simulations, which also enhances the thermoelectric performance.[16]

Many studies have been focused on the importance of external fields in the physical properties of low-dimensional systems. Among them, the staggered exchange field is newly discovered. Including a staggered exchange field and also an external electric field normal to the atomic plane of silicene, the influence of topological edge states and the transition between the topological-insulator and conventional gap-insulator states on the thermoelectric properties, and especially on the spin-related thermoelectric effects has been studied by Wierzbicki *et al.*[17] In the work by Högl *et al.*,[18] it has been shown that the combination of staggered intrinsic spin–orbit and uniform exchange coupling gives topologically protected pseudohelical states. It has also been identified that the staggered damping-like spin–orbit torque is the key mechanism for electrical excitation of the Néel vector in antiferromagnets.[19] Moreover, remarkable quantum phase transitions have been studied in Heisenberg antiferromagnetic chains with staggered power-law decaying long-range interactions.[20] In the case of thermoelectric properties, considering topological and trivial phases of the 2D bismuth layer, the role of edge states has been determined by Gaffar *et al.*[21] Furthermore, the influence of biaxial strain on the group VI elemental 2D material of tellurium has been

[a]Department of Physics and Center for Theoretical and Computational Physics, University of Education, Hue University, Hue 530000, Vietnam. E-mail: buidinhhoi@hueuni.edu.vn

[b]Condensed Matter Theory, TU Dortmund University, Otto-Hahn Straße 4, 44221 Dortmund, Germany

[c]Max-Planck-Institut für Physik komplexer Systeme, Dresden 01187, Germany

investigated, which has been discussed for its potential in thermoelectric applications.[22]

In unconventional QSHIs, so-called noncentrosymmetric QSHIs (NQSHIs), both gapped and gapless states can be protected by the time-reversal symmetry.[23] The unconventionality of these systems is characterized by in-plane spin textures which are controlled by the Rashba SOC (induced by an external electric field).[10,24–26] Usually, heavy atoms are suitable candidates for these properties.[27–31] One of the well-known NQSHIs is monolayer PbBiI, which has recently been proposed theoretically.[23] It demonstrates an unconventional in-plane spin texture with time-reversal symmetry-protected states. When the bulk state is protected by the time-reversal symmetry, the conventional bulk backscattering mechanism is forbidden, which is important for transport in spintronics. Nevertheless, both bulk and edge states in QSHIs can be influenced by internal and external stimuli such as the electron–electron interaction,[32–37] magnetic field,[38–42] and bias field.[1–3]

In this work, we focus on monolayer PbBiI because the backscattering mechanism is forbidden in this material as one of the obstacles of clean transport in a system. Since the effective mass of electrons is of importance in thermoelectric features, electronic transport is much easier in the absence of backscattering. And for this reason, we would propose this monolayer PbBiI as one of the potential systems in the thermoelectric industry. Here, we theoretically increase the thermoelectric PF of the PbBiI compound *via* a staggered exchange field to eventually increase the thermoelectric performance of the system. Here, the staggered exchange field originates from the magnetic proximity effect. The PF is a function of the band dispersion of electrons and for this reason, we modulate the electronic properties to tune $\mathcal{Z}T$. We, in a nutshell, aim at finding novel physical insights for practical thermoelectric applications by observing the effect of unconventional features of NQSHIs in the presence of an external field.

To organize the paper, in Sec. 2, we start with the low-energy Hamiltonian model of PbBiI in the presence of a staggered exchange field. We then use the Kubo–Greenwood (KG) approach to calculate the Onsager transport coefficients required for the PF. Section 3 presents the numerical calculations and we end the paper in Sec. 4 with a summary of the results.

2 Four-band Hamiltonian model

To start, one needs to understand the basic theoretical formulation of monolayer PbBiI, see Fig. 1. The electronic states of this system are characterized by four bands[23] stemming from in-plane and out-of-plane p orbitals of Bi atoms since the role of Pb–I dimers in the effective orbital hybridization of the lattice is negligible. It has been shown that the p_z-Bi orbitals form the highest valence bands, while the lowest conduction bands originate from the $p_{x,y}$-Bi orbitals. For p orbitals, the orbital angular momentum is $L = 1$ and together with the spin angular momentum $S = 1/2$, four effective bands of PbBiI are from the total angular momentum of $J_{1,2} = \{1/2, 3/2\}$ and spin directions

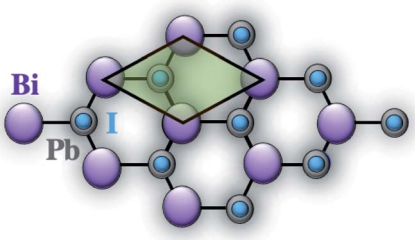

Fig. 1 Top view of monolayer PbBiI. The bond lengths of in-plane Bi–Pb and out-of-plane Pb–I are respectively 3.04 Å and 1.35 Å.[23,43–45] The unit cell is shown by a shaded rhombic.

$m_J = \{+1/2, -1/2\}$.[23,43–45] Based on these states, the tight-binding low-energy Hamiltonian of monolayer PbBiI is given by:[23]

$$\mathscr{H}_{\vec{k}} = \mathscr{H}_0 + \mathscr{H}_{\mathrm{int},\vec{k}}, \tag{1}$$

where $\mathscr{H}_0$ is a diagonal 4×4 matrix with on-site energies $\{-\varepsilon_{1/2}, -\varepsilon_{1/2}, +\varepsilon_{3/2}, +\varepsilon_{3/2}\}$ and

$$\mathscr{H}_{\mathrm{int},\vec{k}} = \begin{pmatrix} \zeta_{1/2}k^2 & \mathrm{i}\alpha_{\mathrm{R},1/2}k_- & 0 & \gamma k_- \\ -\mathrm{i}\alpha_{\mathrm{R},1/2}k_+ & \zeta_{1/2}k^2 & \gamma k_+ & 0 \\ 0 & \gamma k_- & -\zeta_{3/2}k^2 & 0 \\ \gamma k_+ & 0 & 0 & -\zeta_{3/2}k^2 \end{pmatrix}. \tag{2}$$

In the above expression, $k_\pm = k_x \pm \mathrm{i}k_y$ and $k^2 = {k_x}^2 + {k_y}^2$ are momenta and $\varepsilon_{1/2} = 0.1685$ eV, $\varepsilon_{3/2} = 0.1575$ eV, $\zeta_{1/2} = 0.008187$ eV Å^{-2}, $\zeta_{3/2} = 0.038068$ eV Å^{-2}, $\alpha_{\mathrm{R},1/2} = 3.0919$ eV Å^{-1}, and $\gamma = -3.5853$ eV Å^{-1}.[23]

The essential and interesting features of PbBiI electronic states in our work can be generated by an external staggered exchange field. To this end, we update the pristine Hamiltonian through the following exchange field as

$$\mathscr{H}_{\vec{k}} = \mathscr{H}_0 + \mathscr{H}_{\mathrm{int},\vec{k}} - |m_J| \begin{pmatrix} \mathscr{M}_{J_1} & 0 \\ 0 & \mathscr{M}_{J_2} \end{pmatrix} \otimes \sigma_z, \tag{3}$$

where σ_z is the z-component of the Pauli matrix and $\mathscr{M}_{J_i}$ with $i = \{1, 2\}$ is the exchange field, induced by the magnetic proximity effect, for the total angular momentum J_i.[46] For spin-up electrons, first and third diagonal elements are modified by eqn (3), while for spin-down electrons, second and fourth diagonal elements of the Hamiltonian are modified. With the magnetic proximity effect as the source of such a staggered field, we mainly mean staggered exchange magnetization and we would produce such a field through two possible methods. First, we would sandwich PbBiI with two different ferromagnets. Second, we would attach a honeycomb-lattice antiferromagnet[47] or ferrimagnet to PbBiI.

This staggered field originally arises when induced exchange fields acting on two sublattices in a system are different. This is well understood for silicene with a similar buckled structure.[48–50] However, there is a difference between the Kane–Mele models of silicene and PbBiI. Since the matrix elements in the effective Hamiltonian of PbBiI involve only the next nearest

neighbor hopping terms, there are no terms involving nearest-neighbor hopping terms. The Pb–I dimer only mediates the interaction between Bi atoms and its effect is effectively introduced within the next nearest neighbor hopping terms. In contrast, in other buckled honeycomb lattice systems, such as germanene and silicene among others, the nearest neighbor hopping terms are essential to their description. Moreover, in the proposed model the basis is formed by four orbitals per site and in the Kane–Mele model the basis has two orbitals per atom, even if we remove the nearest neighbor contributions in the Kane–Mele model, we would not get the PbBiI effective model. So, this difference introduces a different description of the staggered field in the PbBiI system, which is not the case in other buckled honeycomb lattices. Accordingly, the exchange fields induced into the system through the magnetic proximity effect act on two suborbitals of two different sublattices as one of the possible interactions between orbitals. So, in the real space, it acts similarly on two Bi sublattices but we consider the interaction between different suborbitals for the effective staggered potential.

3 Electronic transport coefficients

In this section, we rely on the KG approach[51,52] to study the thermoelectric PF of monolayer PbBiI in the absence and presence of the external staggered exchange field. In doing so, one needs the charge and thermal currents within the tight-binding framework.[53] We stick to the KG formalism since it is valid for all temperatures.[54] On the other hand, we use the linear response theory for the Onsager transport coefficients[55] in which the currents can be traced by both electric field and temperature gradients. Let us notate the electric field and temperature gradient along the α-direction, respectively, as E_α and $\nabla_\alpha T$. The charge and thermal currents are, respectively, linked to these fields through $\mathscr{J}^{\mathrm{ch}}_{\beta} = \sum_{\alpha}\left(\mathscr{L}^{\alpha\beta}_{11}E^{\alpha} - \frac{\mathscr{L}^{\alpha\beta}_{12}}{eT}\nabla_\alpha T\right)$ and $\mathscr{J}^{\mathrm{th}}_{\beta} = \sum_{\alpha}\left(\mathscr{L}^{\alpha\beta}_{21}E^{\alpha} - \frac{\mathscr{L}^{\alpha\beta}_{22}}{eT}\nabla_\alpha T\right)$[56,57] where e is the electron charge and the Onsager coefficients satisfy the symmetry $\mathscr{L}^{\alpha\beta}_{mn} = \mathscr{L}^{\alpha\beta}_{nm}$ for $\{m, n\} = \{1, 2\}$.

To calculate these transport coefficients, we first calculate the current–current time-correlation functions[51,52,57] with the help of single-particle Green's functions and their time derivatives:

$$\mathscr{L}^{\alpha\beta}_{mn}(\mathrm{i}\omega) = \frac{k_{\mathrm{B}}T}{\mathrm{i}\omega V}\int_0^{1/k_{\mathrm{B}}T} \mathrm{d}\tau \mathrm{e}^{\mathrm{i}\omega\tau}\left\langle T_\tau \mathscr{J}^{\alpha}_{m}(\tau)\mathscr{J}^{\beta}_{n}(0)\right\rangle, \tag{4}$$

where τ is the imaginary time, V is the volume of the system, and $\mathrm{i}\omega$ is the Matsubara frequency.[57] Here we are interested in the static limit of the above equation, *i.e.* the case of $\omega \to 0$, where $\mathscr{L}^{\alpha\beta}_{mn} = \lim_{\omega\to 0}\mathrm{Im}\mathscr{L}^{\alpha\beta}_{mn}(\mathrm{i}\omega\to\omega+\mathrm{i}\delta)$ with the numerical phenomenological parameter $\delta = 1$ meV:

$$\mathscr{L}^{\alpha\beta}_{mn}(T) = \mathscr{C}_{mn}T\int_{-\infty}^{+\infty}\mathrm{d}\mathscr{E}\mathscr{E}^{m+n-2}\mathcal{F}^{\alpha\beta}(\mathscr{E})\partial_{\mathscr{E}}[n_{\mathrm{FD}}(\mathscr{E},T)], \tag{5}$$

$$\mathcal{F}^{\alpha\beta}(\mathscr{E}) = \sum_{\vec{k}}\sum_{\mu,\nu}\nu^{\mu,\nu}_{\vec{k},\alpha}\nu^{\mu,\nu}_{\vec{k},\beta}\mathrm{Im}\left[\mathrm{Tr}G_{\vec{k}}(\mathscr{E})\right]^2, \tag{6}$$

where $\mathscr{C}_{mn} = -\hbar(-e)^{4-m-n}k_{\mathrm{B}}/2V$ and $n_{\mathrm{FD}}(\mathscr{E},T)$ are the Fermi–Dirac distribution functions. Moreover, $G_{\vec{k}}(\mathscr{E}) = [\mathscr{E}+\mathrm{i}\delta-\mathscr{H}_{\vec{k}}]^{-1}$ and $\nu^{\mu,\nu}_{\vec{k},\alpha} = \hbar^{-1}\partial\mathscr{E}^{\mu,\nu}_{\vec{k}}/\partial k_\alpha$ with $\mu = \pm 1$ and $\nu = \pm 1$ for $\{J_1, J_2\}$ and $\{m_J\}$, respectively. Finally, having these coefficients, the thermoelectric PF for an arbitrary direction $\alpha\beta$ reads as

$$\mathcal{P}(T) = \frac{\mathscr{L}^2_{12}(T)}{T^2\mathscr{L}_{11}(T)}. \tag{7}$$

In the following, we immediately present the numerical calculations since the analytical expressions of band dispersions and corresponding charge/thermal current and thermoelectric PF are lengthy.

4 Numerical results

It is necessary to note that the system is isotropic in the absence and presence of a staggered exchange field since the field is an on-site potential and does not act on the off-diagonal elements of the effective Hamiltonian. So, all *xx*, *yy*, and *xy* components of Onsager coefficients are identical. For this reason, we would work with $\mathcal{P}(T)$ in the following at the temperature range 20 K $\leq T \leq$ 1000 K. In general, the size of the bulk band gap, the density of states, and the effective mass (characterized by the concavity of bands) of carriers are the effective parameters to control the PF. For this reason, we first focus on the band dispersions to explore the above features with the exchange field, and secondly, we turn to the PF analysis.

To understand the effects of the staggered exchange field on the PF of PbBiI, we look at the electronic band structure in Fig. 2(a)–(d) and then compare the corresponding PFs in Fig. 2(e). In the first scenario, the exchange field $\mathscr{M}_{J_1}$ is only turned on, implying that the total angular momentum $J = 1/2$ is only included in the electronic transitions. Both the charge and thermal currents are affected by this exchange field because of the changes made in the momentum of host electrons and the spatial distribution of corresponding electronic states (wavefunctions). These, in turn, penetrate the PF. Upon applying the exchange field individually at $\mathscr{M}_{J_1} = 0.2$ eV in Fig. 2(b), only the M-like band (upper band of valence side) and the Λ-like band (lower band of valence side) get away from each other in the vicinity of the Γ-point such that there is no valence band-touching anymore. Correspondingly, see the blue line of Fig. 2(e), the thermopower increases significantly by 32% (from 1.65 to 2.3 μW cm^{-1} K^{-2}) without any temperature shift of PF's shoulder. The larger density of states for the valence bands due to increased concavity and effective mass of carriers are the main reasons for this enhancement. The origin of the broad shoulder near 400 K is, however, the bipolar conduction of carriers. Above this shoulder temperature, the thermal effects are more dominant than the quantum effects and the PF approaches zero.

We find that the contribution of a critical exchange field $\mathscr{M}^{\mathrm{c}}_{J_1} = 2(\varepsilon_{1/2}+\varepsilon_{3/2}) = 0.652$ eV, which only depends on the on-

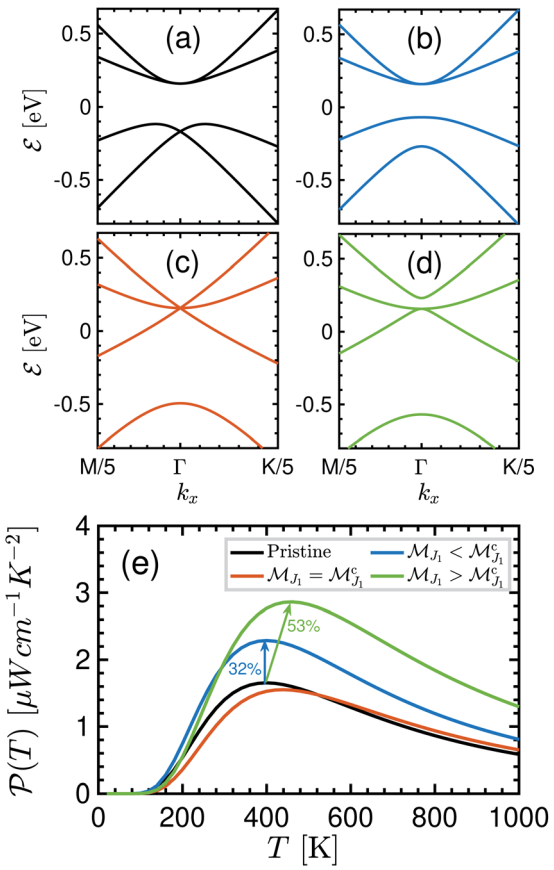

Fig. 2 The electronic band structure of the PbBiI single-layer in the absence (a) $\mathcal{M}_{J_1} = 0$ and presence of respectively individual (b) $\mathcal{M}_{J_1} = 0.2$ eV, (c) $\mathcal{M}_{J_1} = 0.652$ eV, and (d) $\mathcal{M}_{J_1} = 0.8$ eV. Panel (e) indicates the corresponding power factors $\mathcal{P}(T)$ as functions of temperature. The critical individual staggered exchange field for J_i is given by $\mathcal{M}^c_{J_1} = 2(\varepsilon_{1/2} + \varepsilon_{3/2}) = 0.652$ eV.

site potentials of basis states, to the electronic band structure in Fig. 2(c) is the formation of a triplet fermion accompanied by reduction of the contribution of interband transitions to the charge and thermal currents. The triplet fermion effective mass manifests itself on both the PF's shoulder and intensity. Thus, the corresponding PF, see the red line of Fig. 2(e), does not illustrate an enhancement of PF, but it causes a shoulder temperature shift from 400 K to 440 K. The PF is reduced because of the smaller density of states and effective mass of carriers.

However, for $\mathcal{M}_{J_1} = 0.8$ eV in Fig. 2(d), the PF in Fig. 2(e) is significantly increased by 53% (from 1.65 to 2.85 μW cm^{-1} K^{-2}) compared to previous strengths, see the green line. Also, the shoulder temperature is shifted from 400 K to 460 K. The reason can be traced back to the electron-like doped phase of the system since two bands touch each other on the conduction side, which results in a larger density of states and effective mass of carriers in the monolayer PbBiI. The system experiences an electronic phase transition at $\mathcal{M}^c_{J_1}$ and the phases below and above this field are different.

In the next step, we turn on the second exchange field $\mathcal{M}_{J_2}$ in Fig. 3 to act on the total angular momentum $J = 3/2$ including both spins. Similarly, to obtain a comprehensive understanding of the role of $\mathcal{M}_{J_2}$ on the PF, we first explore the evolution of electronic band structure in Fig. 3(a)–(d). In contrast to the previous selection of the exchange field, the second one separates the conduction bands at $\mathcal{M}_{J_2} = 0.2$ eV in Fig. 3(b). The corresponding PF in Fig. 3(e), see the blue line, displays an enhancement of 58% (from 1.65 to 3 μW cm^{-1} K^{-2}) without any temperature shift. We again encounter a critical exchange field $\mathcal{M}^c_{J_2} = 2(\varepsilon_{1/2} + \varepsilon_{3/2}) = 0.652$ eV at which three of four bands touch each other on the valence side in Fig. 3(c) and the triplet fermion is again formed. In contrast to the angular momentum $J = 1/2$, at this strength of perturbation effect for $J = 3/2$, we find 133% (from 1.65 to 8.2 μW cm^{-1} K^{-2}) enhancement of PF in Fig. 3(e), see the red line, associated with a shift of temperature from 400 K to 480 K. In this case, the electronic transitions originate from this point that in our theory, the electronic transitions occur from the valence band to the conduction band and this phenomenon becomes significant with more bands in the valence side when turning on $\mathcal{M}_{J_2}$ such that the density of states and effective mass of carriers reach their maximum values.

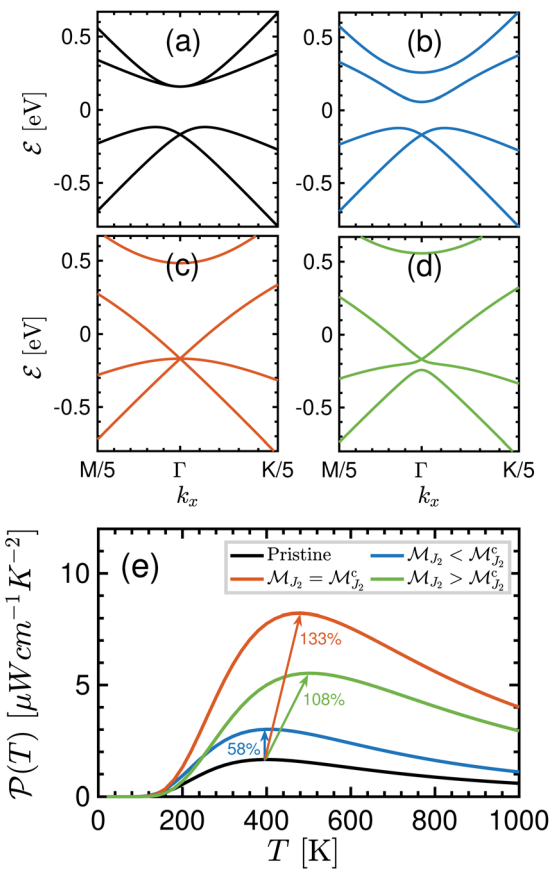

Fig. 3 The electronic band structure of the PbBiI single-layer in the absence (a) $\mathcal{M}_{J_2} = 0$ and presence of respectively individual (b) $\mathcal{M}_{J_2} = 0.2$ eV, (c) $\mathcal{M}_{J_2} = 0.652$ eV, and (d) $\mathcal{M}_{J_2} = 0.8$ eV. Panel (e) indicates the corresponding power factors $\mathcal{P}(T)$ as functions of temperature. The critical individual staggered exchange field for J_i is given by $\mathcal{M}^c_{J_2} = 2(\varepsilon_{1/2} + \varepsilon_{3/2}) = 0.652$ eV.

To gather further evidence, we increase the second field to 0.8 eV in Fig. 3(d) above the critical field. Surprisingly, we find an enhancement of 108% (from 1.65 to 5.6 μW cm^{-1} K^{-2}) for PF in Fig. 3(e), see the green line, compared to the same strength of the first exchange field of Fig. 2(d). As before, the density of states, band dispersion, and effective mass of carriers which are different than the pristine ones lead to such an enhancement with a temperature shift from 400 K to 500 K.

As the last scenario, we will consider dual exchange fields with the options of $\mathcal{M}_{J_1} < \mathcal{M}_{J_2}$ and $\mathcal{M}_{J_1} > \mathcal{M}_{J_2}$ in Fig. 4. Our analysis on the band structure leads to a hole-doped gapless structure at $\mathcal{M}_{J_1} = 0.2$ eV and $\mathcal{M}_{J_2} = 0.45$ eV (blue line in Fig. 4(b)), while an electron-doped gapless structure is obtained at $\mathcal{M}_{J_1} = 0.45$ eV and $\mathcal{M}_{J_2} = 0.2$ eV (red line in Fig. 4(b)) following the inversion symmetry between the exchange fields. Based on the previous argument on the effective electronic transitions from the valence band to the conduction band, one expects a larger enhancement of PF for the first duality option. This is confirmed by the blue line in Fig. 4(c) with 22% (from 1.65 to 2.06 μW cm^{-1} K^{-2}) and 12% (from 1.65 to 1.86 μW cm^{-1} K^{-2}) enhancement, respectively, for the first and second options associated with a temperature shift of 400 K to 420 K and 440 K. However, this last scenario is not yet the proper way compared to the two previous cases.

Note that the negative sign of exchange fields does not affect the results due to the symmetry-protected definition of exchange fields in eqn (3). Also, our investigations do not propose both exchange fields to be turned on simultaneously because this leads to a suppression of PF instead of an enhancement behavior. Finally, we briefly comment on the experimental feasibility of our proposal. To experimentally apply the desired staggered exchange potential in our model, one either can put the PbBiI surface in proximity to a magnetic substrate (*e.g.*, $LaFeO_3$)[58] or can dope the system *via* magnetic atoms (*e.g.* W, Cr, and Mo).[59] As mentioned before, with the magnetic proximity effect as the source of such a staggered field, we would either sandwich PbBiI with two different ferromagnets or would attach a honeycomb-lattice antiferromagnet[47] or ferrimagnet to PbBiI.

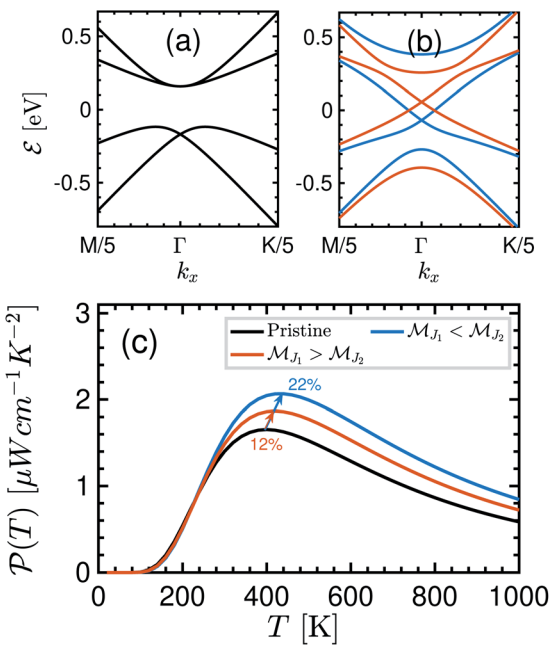

Fig. 4 The electronic band structure of the PbBiI single-layer in the absence (a) $\mathcal{M}_{J_1} = \mathcal{M}_{J_2} = 0$ and presence of dual (b) $\mathcal{M}_{J_1} = 0.2$ eV and $\mathcal{M}_{J_2} = 0.45$ eV (blue lines), and $\mathcal{M}_{J_1} = 0.45$ eV and $\mathcal{M}_{J_2} = 0.2$ eV (red lines). Panel (c) indicates the corresponding power factors $\mathcal{P}(T)$ as functions of temperature.

Table 1 A comparison between the highest PF of monolayer PbBiI (in units of μW cm^{-1} K^{-2}) and other topological materials such as Sn-doped $Bi_{1.1}Sb_{0.9}Te_2S$ (Sn-BSTS),[60] Na_2RbBi,[61] and TCIs[62,63]

T [K]	$\mathcal{P}^{\mathrm{PbBiI}}_{\mathcal{M}_{J_2}=0.8\ \mathrm{eV}}$	$\mathcal{P}^{\mathrm{Sn\text{-}BSTS}}$	$\mathcal{P}^{\mathrm{Na_2RbBi}}$	$\mathcal{P}^{\mathrm{TCI}}$
300	6.00	5.85	2.00	0.40

To highlight the scientific value of the present work, we simply compare the highest obtained PF in monolayer PbBiI with those of other topological materials. In doing so, we use Sn-doped $Bi_{1.1}Sb_{0.9}Te_2S$ (Sn-BSTS),[60] Na_2RbBi,[61] and topological crystalline insulators (TCIs).[62,63] The comparison is shown in Table 1. As can be seen, monolayer PbBiI in the presence of exchange potential $\mathcal{M}_{J_2}$ (because our numerical investigations have already concluded that the effective exchange fields to enhance the PF are the individual ones acting on each total angular momenta with both spins) shows a better thermopower at room temperature compared to the other listed materials.

5 Summary

Time-reversal symmetry-protected bulk and edges states of the PbBiI compound including total angular momenta $J = \{1/2, 3.2\}$ lead to featuring unusual electrical conduction behaviors. Controlling the effective mass of carriers manifests itself in the thermoelectric performance of the system. In this paper, we have aimed at manipulating the electronic band structure of PbBiI by a proposed staggered exchange field to enhance its thermoelectric PF. A low-energy Hamiltonian model is implemented within the Kubo–Greenwood formalism to calculate the electronic transport coefficients and the PF later. We demonstrate that an optimal exchange field 0.652 eV, 0.8 eV, and {0.2, 0.45} eV acting on $J = 3/2$, $J = 1/2$ and both Js results in a significant enhancement of thermoelectric PF due to highly dispersive and degenerated energy bands. The enhancement of PF at the temperatures 480 K, 460 K, and 440 K for the above momenta are, respectively, about 133%, 53%, and 22%. This work is valuable in the confirmation that there is a simple way to increase the thermoelectric performance of PbBiI.

Conflicts of interest

There are no conflicts to declare.

Acknowledgements

This research is funded by the Vietnam National Foundation for Science and Technology Development (NAFOSTED) under grant number 103.01-2020.61. M. Yarmohammadi gratefully acknowledges financial support by the DFG (German Science Foundation) in Grant No. UH 90/13-1.

References

1 C. L. Kane and E. J. Mele, *Phys. Rev. Lett.*, 2005, **95**, 226801.
2 B. A. Bernevig, T. L. Hughes and S.-C. Zhang, *Science*, 2006, **314**, 1757–1761.
3 M. König, S. Wiedmann, C. Brüne, A. Roth, H. Buhmann, L. W. Molenkamp, X.-L. Qi and S.-C. Zhang, *Science*, 2007, **318**, 766–770.
4 L. Kou, Y. Ma, Z. Sun, T. Heine and C. Chen, *J. Phys. Chem. Lett.*, 2017, **8**, 1905–1919.
5 L. Müchler, H. Zhang, S. Chadov, B. Yan, F. Casper, J. Kübler, S.-C. Zhang and C. Felser, *Angew. Chem., Int. Ed.*, 2012, **51**, 7221–7225.
6 D. Kong and Y. Cui, *Nat. Chem.*, 2011, **3**, 845–849.
7 S.-Y. Xu, C. Liu, N. Alidoust, M. Neupane, D. Qian, I. Belopolski, J. D. Denlinger, Y. J. Wang, H. Lin, L. A. Wray, G. Landolt, B. Slomski, J. H. Dil, A. Marcinkova, E. Morosan, Q. Gibson, R. Sankar, F. C. Chou, R. J. Cava, A. Bansil and M. Z. Hasan, *Nat. Commun.*, 2012, **3**, 1192.
8 X. Wang, Y. Du, S. Dou and C. Zhang, *Phys. Rev. Lett.*, 2012, **108**, 266806.
9 M. Z. Hasan and C. L. Kane, *Rev. Mod. Phys.*, 2010, **82**, 3045–3067.
10 X.-L. Qi and S.-C. Zhang, *Rev. Mod. Phys.*, 2011, **83**, 1057–1110.
11 B. Yan and S.-C. Zhang, *Rep. Prog. Phys.*, 2012, **75**, 096501.
12 F. J. DiSalvo, *Science*, 1999, **285**, 703–706.
13 G. J. Snyder and E. S. Toberer, in *Complex Thermoelectric Materials*, 2011, pp. 101–110.
14 Z. Ding, M. An, S. Mo, X. Yu, Z. Jin, Y. Liao, K. Esfarjani, J.-T. Lü, J. Shiomi and N. Yang, *J. Mater. Chem. A*, 2019, **7**, 2114–2121.
15 X.-Y. Mi, X. Yu, K.-L. Yao, X. Huang, N. Yang and J.-T. Lü, *Nano Lett.*, 2015, **15**, 5229–5234.
16 X. Yu, R. Li, T. Shiga, L. Feng, M. An, L. Zhang, J. Shiomi and N. Yang, *J. Phys. Chem. C*, 2019, **123**, 26735–26741.
17 M. Wierzbicki, J. Barnaś and R. Swirkowicz, *Phys. Rev. B: Condens. Matter Mater. Phys.*, 2015, **91**, 165417.
18 P. Högl, T. Frank, K. Zollner, D. Kochan, M. Gmitra and J. Fabian, *Phys. Rev. Lett.*, 2020, **124**, 136403.
19 F. Xue and P. M. Haney, *Phys. Rev. B*, 2021, **104**, 224414.
20 J. Ren, Z. Wang, W. Chen and W.-L. You, *Phys. Rev. E*, 2022, **105**, 034128.
21 M. Gaffar, S. A. Wella and E. H. Hasdeo, *Phys. Rev. B*, 2021, **104**, 205105.
22 S. Karmakar and T. Saha-Dasgupta, *Phys. Rev. Mater.*, 2021, **5**, 124006.
23 C. Mera Acosta, O. Babilonia, L. Abdalla and A. Fazzio, *Phys. Rev. B*, 2016, **94**, 041302.
24 S. Maekawa, S. Valenzuela, E. Saitoh and T. Kimura, *Spin Current*, OUP, Oxford, 2012.
25 A. Manchon, H. C. Koo, J. Nitta, S. M. Frolov and R. A. Duine, *Nat. Mater.*, 2015, **14**, 871–882.
26 D. Bercioux and P. Lucignano, *Rep. Prog. Phys.*, 2015, **78**, 106001.
27 J. Nitta, T. Akazaki, H. Takayanagi and T. Enoki, *Phys. Rev. Lett.*, 1997, **78**, 1335–1338.
28 T. Hirahara, T. Nagao, I. Matsuda, G. Bihlmayer, E. V. Chulkov, Y. M. Koroteev, P. M. Echenique, M. Saito and S. Hasegawa, *Phys. Rev. Lett.*, 2006, **97**, 146803.
29 S. Mathias, A. Ruffing, F. Deicke, M. Wiesenmayer, I. Sakar, G. Bihlmayer, E. V. Chulkov, Y. M. Koroteev, P. M. Echenique, M. Bauer and M. Aeschlimann, *Phys. Rev. Lett.*, 2010, **104**, 066802.
30 H. Yuan, M. S. Bahramy, K. Morimoto, S. Wu, K. Nomura, B.-J. Yang, H. Shimotani, R. Suzuki, M. Toh, C. Kloc, X. Xu, R. Arita, N. Nagaosa and Y. Iwasa, *Nat. Phys.*, 2013, **9**, 563–569.
31 J. H. Dil, F. Meier, J. Lobo-Checa, L. Patthey, G. Bihlmayer and J. Osterwalder, *Phys. Rev. Lett.*, 2008, **101**, 266802.
32 J. C. Budich, F. Dolcini, P. Recher and B. Trauzettel, *Phys. Rev. Lett.*, 2012, **108**, 086602.
33 F. m. c. Crépin, J. C. Budich, F. Dolcini, P. Recher and B. Trauzettel, *Phys. Rev. B: Condens. Matter Mater. Phys.*, 2012, **86**, 121106.
34 T. L. Schmidt, S. Rachel, F. von Oppen and L. I. Glazman, *Phys. Rev. Lett.*, 2012, **108**, 156402.
35 J. I. Väyrynen, M. Goldstein and L. I. Glazman, *Phys. Rev. Lett.*, 2013, **110**, 216402.
36 F. Geissler, F. m. c. Crépin and B. Trauzettel, *Phys. Rev. B: Condens. Matter Mater. Phys.*, 2014, **89**, 235136.
37 K. Jiang, S. Zhou, X. Dai and Z. Wang, *Phys. Rev. Lett.*, 2018, **120**, 157205.
38 M. König, H. Buhmann, L. W. Molenkamp, T. Hughes, C.-X. Liu, X.-L. Qi and S.-C. Zhang, *J. Phys. Soc. Jpn.*, 2008, **77**, 031007.
39 B. Scharf, A. Matos-Abiague and J. Fabian, *Phys. Rev. B: Condens. Matter Mater. Phys.*, 2012, **86**, 075418.
40 P. Debray, S. M. S. Rahman, J. Wan, R. S. Newrock, M. Cahay, A. T. Ngo, S. E. Ulloa, S. T. Herbert, M. Muhammad and M. Johnson, *Nat. Nanotechnol.*, 2009, **4**, 759–764.
41 P. Chuang, S.-C. Ho, L. W. Smith, F. Sfigakis, M. Pepper, C.-H. Chen, J.-C. Fan, J. P. Griffiths, I. Farrer, H. E. Beere, G. A. C. Jones, D. A. Ritchie and T.-M. Chen, *Nat. Nanotechnol.*, 2015, **10**, 35–39.
42 A. T. Ngo, P. Debray and S. E. Ulloa, *Phys. Rev. B: Condens. Matter Mater. Phys.*, 2010, **81**, 115328.
43 R. Yu, X. L. Qi, A. Bernevig, Z. Fang and X. Dai, *Phys. Rev. B: Condens. Matter Mater. Phys.*, 2011, **84**, 075119.
44 A. A. Soluyanov and D. Vanderbilt, *Phys. Rev. B: Condens. Matter Mater. Phys.*, 2011, **83**, 035108.
45 A. A. Soluyanov and D. Vanderbilt, *Phys. Rev. B: Condens. Matter Mater. Phys.*, 2011, **83**, 235401.
46 G. Xu, T. Zhou, B. Scharf and I. Žutić, *Phys. Rev. Lett.*, 2020, **125**, 157402.

47 X. Li, T. Cao, Q. Niu, J. Shi and J. Feng, *Proc. Natl. Acad. Sci.*, 2013, **110**, 3738–3742.
48 M. Ezawa, *New J. Phys.*, 2012, **14**, 033003.
49 M. Ezawa, *Phys. Rev. B: Condens. Matter Mater. Phys.*, 2013, **87**, 155415.
50 M. Ezawa and N. Nagaosa, *Phys. Rev. B: Condens. Matter Mater. Phys.*, 2013, **88**, 121401.
51 R. Kubo, *J. Phys. Soc. Jpn.*, 1957, **12**, 570–586.
52 D. A. Greenwood, *Proc. Phys. Soc.*, 1958, **71**, 585–596.
53 I. Paul and G. Kotliar, *Phys. Rev. B: Condens. Matter Mater. Phys.*, 2003, **67**, 115131.
54 B. Holst, M. French and R. Redmer, *Phys. Rev. B: Condens. Matter Mater. Phys.*, 2011, **83**, 235120.
55 L. Onsager, *Phys. Rev.*, 1931, **37**, 405–426.
56 H. Callen, N. F. R. C. of Australia. Research Division and W. Sons, *Thermodynamics and an Introduction to Thermostatistics*, Wiley, 1985.
57 G. Mahan, *Many-Particle Physics*, Springer US, 2000.
58 T. Zhou, J. Zhang, Y. Xue, B. Zhao, H. Zhang, H. Jiang and Z. Yang, *Phys. Rev. B*, 2016, **94**, 235449.
59 T. Zhou, J. Zhang, B. Zhao, H. Zhang and Z. Yang, *Nano Lett.*, 2015, **15**, 5149–5155.
60 S. Y. Matsushita, K. Ichimura, K. K. Huynh and K. Tanigaki, *Phys. Rev. Mater.*, 2021, **5**, 014205.
61 S. Yalameha, Z. Nourbakhsh and D. Vashaee, *J. Phys.: Condens. Matter*, 2021, **34**, 105702.
62 L.-D. Zhao, G. Tan, S. Hao, J. He, Y. Pei, H. Chi, H. Wang, S. Gong, H. Xu, V. P. Dravid, C. Uher, G. J. Snyder, C. Wolverton and M. G. Kanatzidis, *Science*, 2016, **351**, 141–144.
63 C. Guo, D. Wang, X. Zhang and L.-D. Zhao, *Chem. Mater.*, 2022, **34**, 3423–3429.

